remote sensing

MDPI

Article

Integration of InSAR and GNSS Data: Improved Precision and Spatial Resolution of 3D Deformation

Xiaoyong Wu [1,2], Yun Shao [3], Zimeng Yang [3], Lihua Lan [4], Xiaolin Bian [1,3] and Ming Liu [3,*]

[1] Aerospace Information Research Institute, Chinese Academy of Sciences, Beijing 100094, China; xywu@aircas.ac.cn (X.W.)
[2] University of Chinese Academy of Sciences, Beijing 100049, China
[3] Laboratory for Microwave Spatial Intelligence and Cloud Platform, Deqing Academy of Satellite Applications, Huzhou 313200, China
[4] Institute of Geographic Sciences and Natural Resources Research, Chinese Academy of Sciences, Beijing 100101, China
* Correspondence: euler@dasa.net.cn

Highlights

What are the main findings?

- A high-resolution three-dimensional (3D) surface velocity map was achieved by integrating InSAR and GNSS data.
- The InSAR velocity was tied to the stable Eurasian reference frame adopted by GNSS, so that the two data can be directly compared.

What are the implications of the main findings?

- A sharp velocity gradient extending ~45 km along the strike of the Laohushan segment of the Haiyuan Fault, with a differential movement of ~3 mm/a across the fault, was observed in the east–west velocity component, reflecting shallow aseismic slip.
- Subsidence caused by hydrological and anthropogenic processes presented distinct characteristics in the vertical velocity.

Abstract

High-precision and high-resolution surface deformation provide crucial constraints for studying the kinematic characteristics and dynamic mechanisms of crustal movement. Considering the limitations of existing geodetic observations, we used Sentinel-1 SAR images and accurate GNSS velocity to obtain a high-resolution three-dimensional (3D) surface velocity map across the Laohushan segment and the 1920 Haiyuan earthquake rupture zone of the Haiyuan Fault on the northeastern Tibetan Plateau. We tied the InSAR LOS (Line of Sight) velocity to the stable Eurasian reference frame adopted by GNSS. Using Kriging interpolation constrained by GNSS north–south components, we decomposed the ascending and descending InSAR velocities into east–west and vertical components to derive a high-resolution 3D deformation. We found that a sharp velocity gradient extending ~45 km along the strike of the Laohushan segment, with a differential movement of ~3 mm/a across the fault, manifests in the east–west velocity component, suggesting that shallow creep has propagated to the surface. However, the east–west velocity component did not exhibit an abrupt discontinuity in the rupture zone of the Haiyuan earthquake. Subsidence caused by anthropogenic and hydrological processes in the region, such as groundwater extraction, coal mining, and hydrologic effects, exhibited distinct distribution characteristics in the vertical velocity component. Our study provides valuable insights into the crustal movement in this region.

Check for updates

Academic Editors: Antonio Miguel Ruiz Armenteros and Ionut Sandric

Received: 12 August 2025
Revised: 14 November 2025
Accepted: 1 December 2025
Published: 1 January 2026

Copyright: © 2026 by the authors. Licensee MDPI, Basel, Switzerland. This article is an open access article distributed under the terms and conditions of the Creative Commons Attribution (CC BY) license.

Keywords: Integration; InSAR; GNSS; 3D deformation; Eurasian reference frame; Subsidence; Haiyuan Fault; Shallow creep

1. Introduction

Precise and accurate terrestrial geodetic measurements serve as crucial constraints for investigating the kinematic characteristics and dynamic mechanisms of crustal deformation [1–3]. Conventionally, leveling, triangulation, and trilateration have long been used to monitor surface deformation with high cost, low efficiency, and restriction in spatial scale and coverage, which limit their widespread deployment [4]. In the past three decades, advancements in space geodesy, such as Interferometric Synthetic Aperture Radar (InSAR) and Global Navigation Satellite System (GNSS), have significantly improved the precision and accuracy of surface deformation measurements, providing unprecedented insight into the characterization of crustal deformation caused by hydrological and anthropogenic processes and tectonic movements [3–10]. It is now possible to continuously monitor earthquakes [11–15], volcanoes [16], landslides [17], plate motions [18–20], permafrost [21,22], and land subsidence [23–27]. Despite its advantages, InSAR is only capable of obtaining the projection of three-dimensional surface deformation along the line of sight (LOS) of the satellite [28], increasing the difficulty of interpreting surface deformation. Moreover, it is particularly insensitive to displacement in the north–south direction, owing to the satellite's near-polar orbit and side-looking geometry [29]. Additionally, GNSS in situ measurements are sparse, making their interpolation inaccurate. Furthermore, the InSAR and GNSS velocity estimates are referenced to different frames, which complicates their direct comparison. Integrating InSAR and GNSS data is desirable to better tackle such a challenging problem, allowing for the complementary advantages of both technologies to achieve consistent deformation results [11,12,30–32] and enabling high-resolution 3D deformation measurements [33–39].

The Haiyuan Fault (HYF), a major active strike–slip structure consisting of a few tens-of-kilometers-long segments on the northeastern margin of the Tibetan Plateau, spans ~1000 km between the Qilian Mountains to the west and the Qinling Mountains to the east (Figure 1) [40–42]. It was the source of the 1920 Haiyuan Mw7.9 earthquake [40] and is critical for accommodating crustal deformation and kinematic transitions in the region [41,42]. Over the past few decades, numerous geodetic investigations using InSAR and GNSS have estimated the slip rate and locking depth along the Haiyuan Fault [43–53]. It is worth highlighting that jointly constraining parameter inversion from InSAR and GNSS data can significantly improve the resolution and robustness of kinematic models [50–54]. Although faults are typically locked in the upper crust, accumulating elastic strain and then releasing it during seismic slip, the Laohushan segment of the Haiyuan Fault undergoes aseismic slip, known as creep [43–51]. However, details of the distribution of creep in space have not yet been resolved. Additionally, subsidence caused by anthropogenic and hydrological processes in the region exhibits complex distribution characteristics [54–56], rendering it difficult to accurately capture tectonic signals. Therefore, the 3D velocity decomposed from InSAR velocity is beneficial for distinguishing different signals.

To achieve high-precision and high-resolution 3D surface deformation across the Laohushan section and the Haiyuan earthquake rupture zone of the Haiyuan Fault, we first conduct a time series analysis of Sentinel-1 SAR images using InSAR technology. The InSAR velocity was then tied to the stable Eurasian reference framework based on the recently published GNSS velocity in China [57,58]. Finally, after removing the interpolated

GNSS south–north component, we decomposed the InSAR velocity residual into east–west and vertical components, with the associated uncertainties discussed.

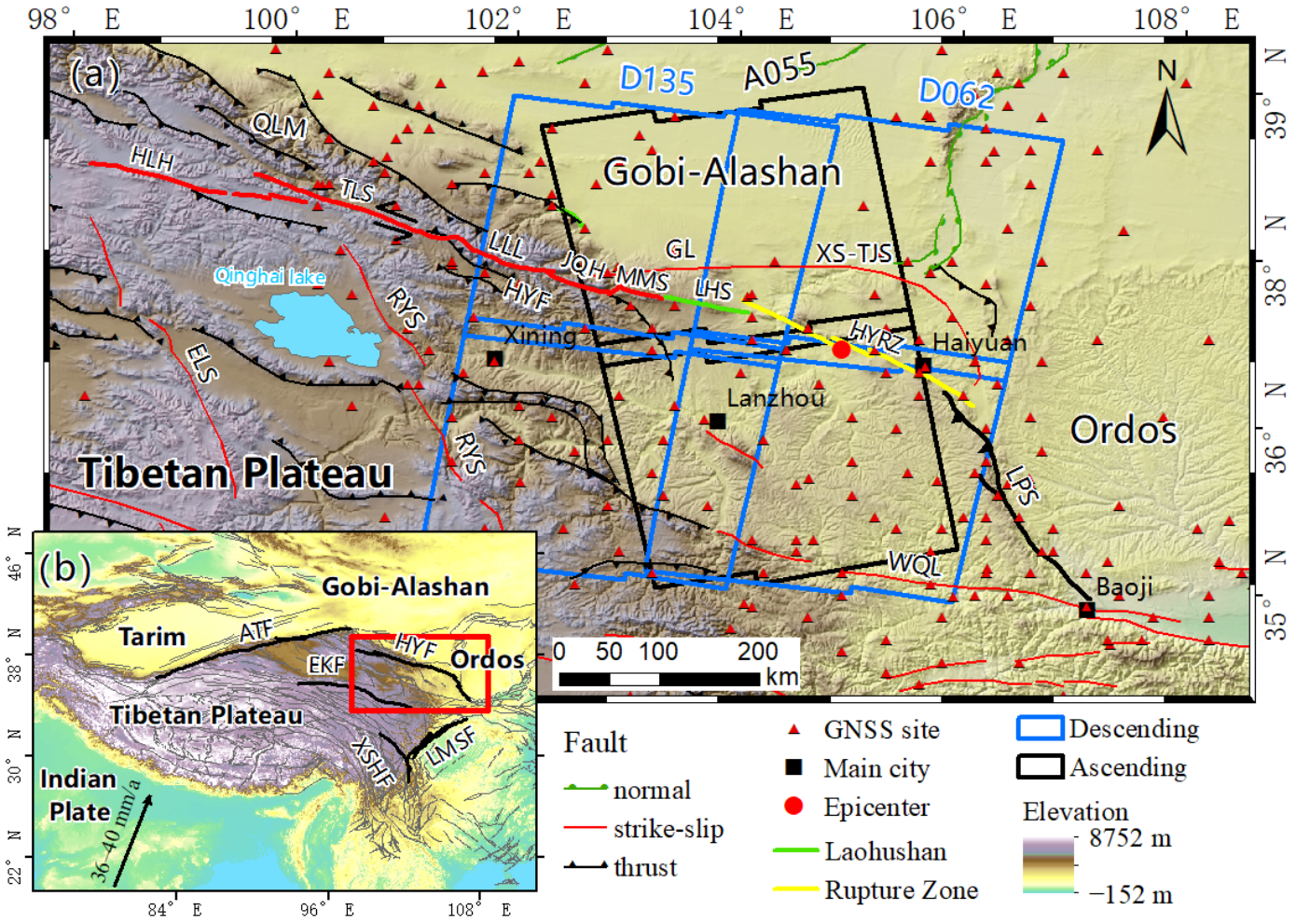


Figure 1. Tectonic setting of the study area overlain on a shaded-relief topography [59]. (**a**) Main active faults [60] of the study area. Thick green and yellow lines highlight the Laohushan segment and the 1920 Haiyuan earthquake rupture zone of the Haiyuan Fault [61], respectively. Red triangles denote GNSS sites [57,58]. Black and blue polygons show the footprints of ascending and descending Sentinel-1 images, respectively. (**b**) Topography and fault traces [60] of the India–Eurasia collision zone. Red rectangle in (**b**) highlights the regional location of the main figure (**a**). ATF: Altyn Tagh Fault; EKF: East Kunlun Fault; ELS: Elashan; GL: Gulang; HYF: Haiyuan Fault; HYRZ: Haiyuan Rupture Zone; HLH: Halahu; JQH: Jinqianghe; LMSF: Longmenshan Fault; LLL: Lenglongling; LHS: Laohushan; LPS: Liupanshan; MMS: Maomaoshan; QLM: Qilian Mountain; RYS: Riyueshan; TLS: Tuolaishan; WQL: Western Qinling; XSHF: Xianshuihe Fault; XS-TJS: Xiangshan–Tianjingshan.

2. Materials and Methods

2.1. InSAR and GNSS Data

The SLC (Single Look Complex) images of Sentinel-1 IW (Interferometric Wide) swath mode, which cover three paths and a total of 457 images, including 153 ascending (A055) and 304 descending (D062 and D135) images, were used in this study (Table 1). Almost all paths were observed for approximately six years, spanning 2014 to 2020. The majority of images had a revisit period of 12 days, and the perpendicular baseline was mainly within ± 150 m, ensuring good coherence (Figure S1).

Table 1. Sentinel-1 SLC image lists used in this study.

Path [1]	Frame	Beam Mode	Number of Image	Time Span
D135	466–477	IW	149	26 October 2014–12 September 2020
D062	466–476	IW	155	9 October 2014–19 September 2020
A055	114–125	IW	153	21 October 2014–19 September 2020

[1] D: Descending, A: Ascending.

Moreover, the Crustal Movement Observation Network of China (CMONOC) has achieved significant research findings in monitoring major tectonic blocks, active faults, and seismic hazard zones across China after nearly three decades of construction and development [5,57,58,62,63]. This study utilized the most recent GNSS velocity published by Wang and Shen [57] (Figure 2), which incorporated 25 years of GNSS observations and removed the effects of seasonal variations, as well as coseismic and postseismic deformation caused by large earthquakes, thus ensuring the reliability of velocity and reflecting relatively stable long-term tectonic deformation. In addition, Liang et al. [58] published three-dimensional GNSS velocities. In this study, we used only the vertical component of Liang et al. [58].

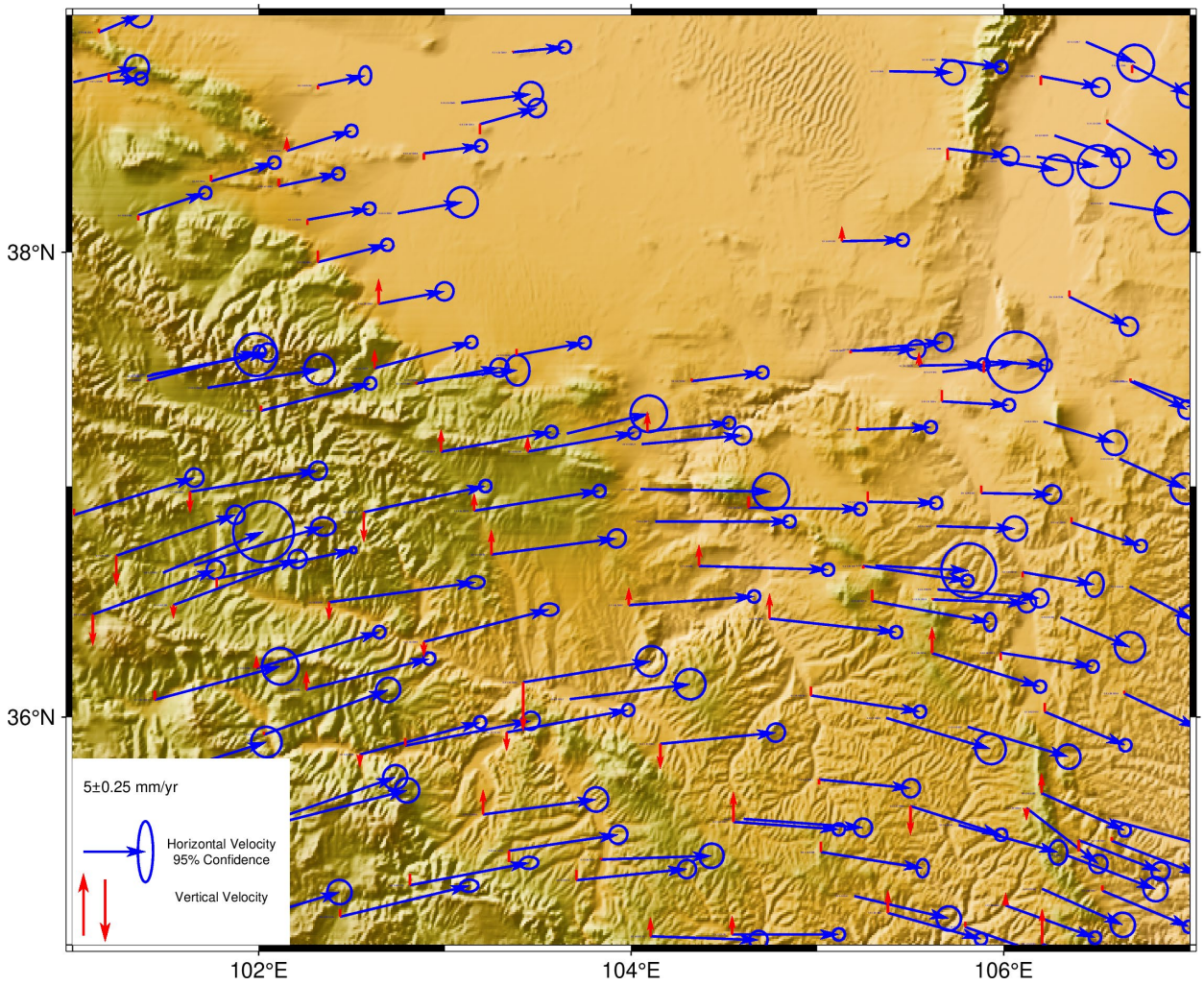


Figure 2. GNSS three-dimensional velocities. The blue arrows represent the GNSS horizontal velocity [57], with ellipses indicating the 1 sigma uncertainty at a 95% confidence level. The red arrows represent the vertical velocity [58], with upward and downward arrows indicating uplift and subsidence, respectively. The image was generated using GMT v6.4.0 [64].

2.2. InSAR Processing

The ISCE2 (InSAR Scientific Computing Environment) v2.6.1 topsStack processor [65,66] developed at JPL/Caltech was used to generate interferograms with 21 and 7 looks in the range and azimuth directions, respectively. The 30 m resolution Shuttle Radar Topography Mission (SRTM) Digital Elevation Model (DEM) [59] and Precise Orbit data were employed to simulate and remove the topographic and flat-earth phases from each interferogram. Then, the statistical-cost network-flow algorithm (SNAPHU) [67] was applied to unwrap the phases of the coregistered interferograms. Finally, we obtained a stack of phase-unwrapped interferograms coregistered to a common SAR acquisition, corrected for earth curvature and topography, which were then used to estimate the average LOS velocity (Figure 3).

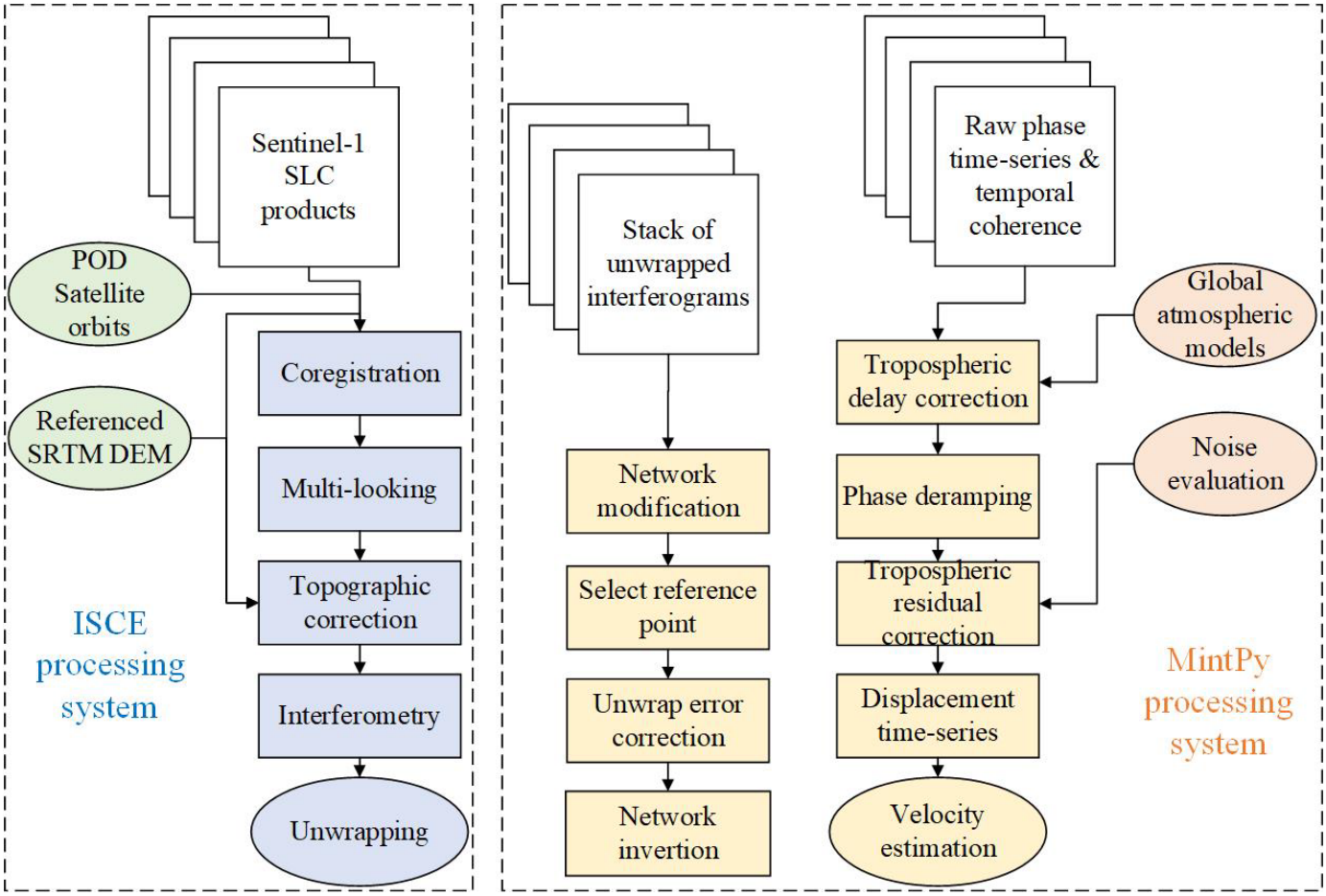


Figure 3. Routine workflow of InSAR processing from Sentinel-1 SLC products to time series. The dashed box on the left shows the ISCE processing flow, which involves registering Sentinel-1 SLC images and performing multi-looking. With the assistance of external DEM and satellite orbit data, the topographic and flat phases were removed to generate interferograms for phase unwrapping. The dashed box on the right shows the MintPy v1.6.1 processing flow, which performs unwrapping error correction and network inversion on a stack of unwrapped interferograms. The global atmospheric model and noise estimation were used to correct the tropospheric delay and tropospheric residual, respectively, to obtain the displacement time series and generate the average velocity.

The MintPy (Miami InSAR time series software in Python) v1.6.1 [68], an open-source tool, was used for the InSAR time series analysis. It incorporates a distributed scatterer approach and an enhanced small baseline subsets (SBAS) algorithm [69]. In contrast to the traditional interferogram domain, MintPy employs a fully connected network of interferograms with phase corrections in the time series domain. Following the routine

workflow of the InSAR time series analysis, the interferogram stack was first inverted for the raw phase time series. Subsequently, noise-reduced displacement time series were obtained by correcting for tropospheric delays using a global atmospheric model [70,71], topographic residuals, and/or a phase ramp. The average LOS velocity was then estimated using the noise-reduced displacement time series for each pixel (Figure 3).

2.3. Velocity Decomposition

Assuming that the direction in which the satellite points towards the ground target is positive, the geometric relationship between the ascending and descending satellite LOS and three-dimensional deformation (Figure 4) can be expressed as follows:

$$\begin{aligned} V_{LOS}^{A} &= V_E \cdot sin\left(\alpha^A - \tfrac{3\pi}{2}\right) \cdot sin\theta^A + V_N \cdot cos\left(\alpha^A - \tfrac{3\pi}{2}\right) \cdot sin\theta^A - V_U \cdot cos\theta^A \\ &= V_E \cdot cos\alpha^A \cdot sin\theta^A - V_N \cdot sin\alpha^A \cdot sin\theta^A - V_U \cdot cos\theta^A \end{aligned} \quad (1)$$

$$\begin{aligned} V_{LOS}^{D} &= -V_E \cdot cos\left(\alpha^D - \pi\right) \cdot sin\theta^D + V_N \cdot sin\left(\alpha^D - \pi\right) \cdot sin\theta^D - V_U \cdot cos\theta^D \\ &= V_E \cdot cos\alpha^D \cdot sin\theta^D - V_N \cdot sin\alpha^D \cdot sin\theta^D - V_U \cdot cos\theta^D \end{aligned} \quad (2)$$

where V_{LOS} is the LOS velocity; θ is the local incidence angle of Radar; α is the azimuth along the satellite heading; A and D indicate ascending and descending, respectively; and $\begin{bmatrix} V_E & V_N & V_U \end{bmatrix}^T$ represent the eastward, northward, and vertical velocity components, respectively.

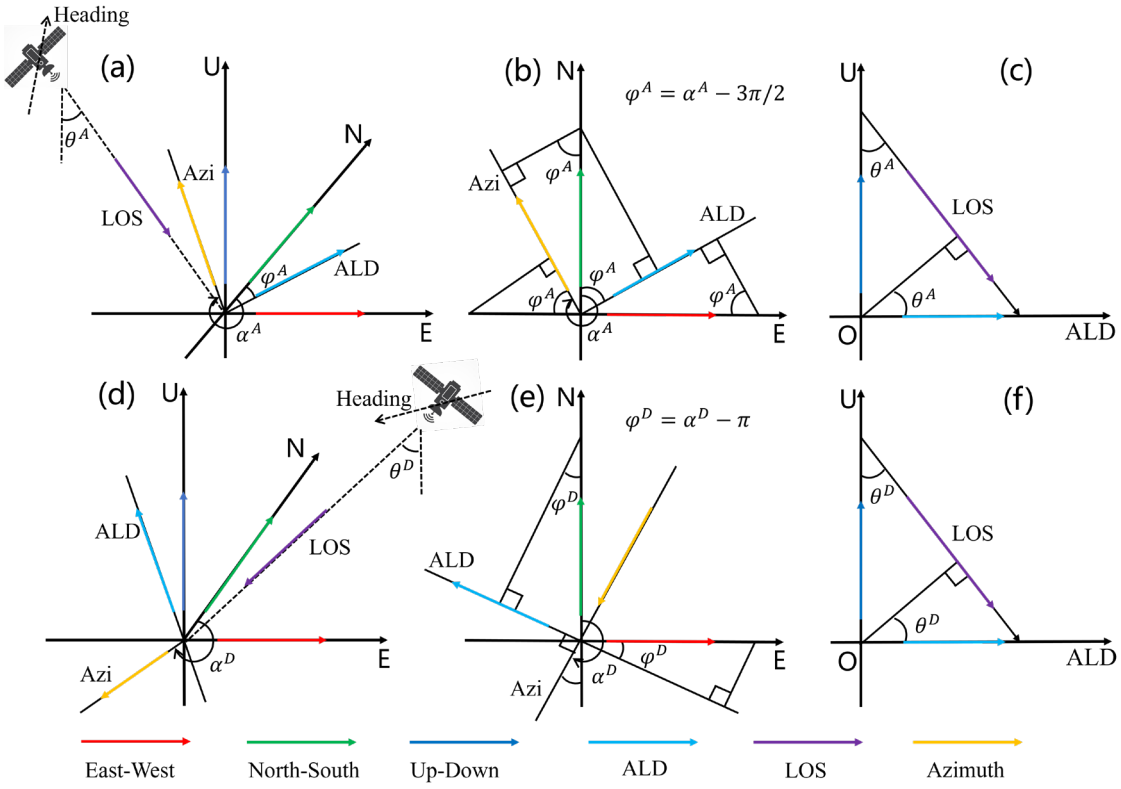


Figure 4. Geometric relationship between satellite LOS and three-dimensional deformation of ground target. Ascending (**a**–**c**) and descending (**d**–**f**) geometry: (**a**,**d**) 3D view, (**b**,**e**) horizontal, (**c**,**f**) vertical. E, N, and U represent east, north, and vertical direction, respectively. Azimuth (Azi) is the satellite flight azimuth direction, and Azimuth Look Direction (ALD) indicates the projection of the satellite LOS on the ground.

Therefore, the geometric relationship between the satellite LOS and three-dimensional deformation can be expressed as follows [29]:

$$V_{LOS} = \begin{bmatrix} sin(\theta)cos(\alpha) & -sin(\theta)sin(\alpha) & -cos(\theta) \end{bmatrix} \begin{bmatrix} V_E \\ V_U \\ V_U \end{bmatrix} \quad (3)$$

It is worth noting that if we assume that the direction from the ground target to the satellite is positive, then the corresponding sign in Equations (1)–(3) should be inverted (i.e., multiplied by -1) to maintain consistency with the coordinate system definition (Figure 4). We can combine the InSAR LOS velocities at the same ground location but with different view directions to obtain the 3D velocity components of ground motion, namely, the east–west, north–south, and vertical components [29]. Because we have two observations (i.e., the LOS velocities for satellite ascending and descending tracks), but the equation has three unknowns (i.e., the three velocity components), this system of equations is underdetermined. Therefore, to obtain a unique solution to the equation, we must add an additional observation to the equation or impose a prior constraint on one of the parameters of the equation. Here, we utilized the GNSS north–south component velocity to compensate for the deficiency of satellite LOS measurements, which are insensitive to north–south movements.

We used the Universal Kriging algorithm to interpolate the GNSS north–south velocity, which can simultaneously obtain the uncertainty of the interpolated velocity. We chose to remove a second-order polynomial surface that describes the distribution of the GNSS north–south velocity. To reduce the impact of measurement errors on the experimental results, we removed stations with vertical velocity standard deviations greater than 1 mm/a. To determine the weight of distance-dependent data points during the interpolation process, we calculated the empirical semivariogram [72] for the detrended GNSS north–south velocity and selected a spherical model [54] for the parameter fitting of the semivariogram. The spherical model determines how uncertainty increases with station distance. The empirical semivariogram and spherical model are expressed as follows:

$$\gamma(h) = \frac{1}{2N}\sum_{i=1}^{N}[Q(x_{i+h}) - Q(x_i)]^2 \quad (4)$$

$$C(h) = \begin{cases} n + (s-n) \times \left(\frac{3h}{2r} - \frac{h^3}{2r^3}\right), & h \le r \\ n + (s-n), & h > r \end{cases} \quad (5)$$

where x and Q are the observation point (i.e., GNSS stations) position and value, respectively. N is the number of pairs of observation points; h is the distance between any pair of observation points; γ is the semivariogram; n is the nugget constant; s is the sill value; r is the range; and C is the covariance function.

Subsequently, the GNSS north–south component velocity projected onto the LOS direction was removed from each track, leaving the LOS velocity solely composed of the east and vertical components. Therefore, for pixels with both ascending and descending LOS displacements, the eastward and vertical velocity components were obtained simultaneously by solving a system of linear equations, namely the following:

$$\begin{bmatrix} V_{LOS}^A - V_{LOS}^N \\ V_{LOS}^D - V_{LOS}^N \end{bmatrix} = \begin{bmatrix} sin(\theta^A)cos(\alpha^A) & -cos(\theta^A) \\ sin(\theta^D)cos(\alpha^D) & -cos(\theta^D) \end{bmatrix} \begin{bmatrix} V_E \\ V_U \end{bmatrix} \quad (6)$$

We used weighted least squares and the variance–covariance matrix (VCM) of the observed data to estimate the uncertainties of velocities V_E and V_U. The observed data

VCM is a 2-by-2 matrix, with variance values for each given point in each track along the main diagonal. Assuming no correlation between the tracks, the non-diagonal values of the VCM are 0. The uncertainties of the eastward and vertical velocities can be expressed as follows [73]:

$$Q_m = \left(G'WG\right)^{-1} \quad (7)$$

where Q_m is a 2-by-2 VCM, G is the design matrix (a 2-by-2 matrix in the above formula), and W is the inverse of the observed data VCM.

3. Results

3.1. InSAR LOS Velocity

The InSAR LOS velocities are shown in Figure 5, with positive values (i.e., warm color) indicating that the ground targets move toward the satellite, and negative values (i.e., cold color) indicating that the ground targets move away from the satellite. The color difference in the LOS velocity across the Haiyuan Fault indicates differential movement across it, reflecting that the fault primarily exhibits strike–slip motions. Furthermore, considering the geometry of the satellite ascending and descending tracks, the above velocity characteristics are consistent with the sinistral strike–slip of the fault. Similar characteristics have also been observed on other major strike–slip faults, such as the North Anatolian Fault [74–78] and the San Andreas Fault [11,12,34]. However, InSAR measures the one-dimensional displacement of ground targets in the satellite's LOS direction, which is the projection of the three-dimensional motion of ground targets in the horizontal and vertical directions onto the LOS direction [29]. Because InSAR LOS velocities are relative observations, meaning that the initial LOS velocities in each frame are referenced to a relatively stable pixel (Figures 5 and S2), they reflect displacement changes relative to the reference point and cannot directly reflect true surface deformation.

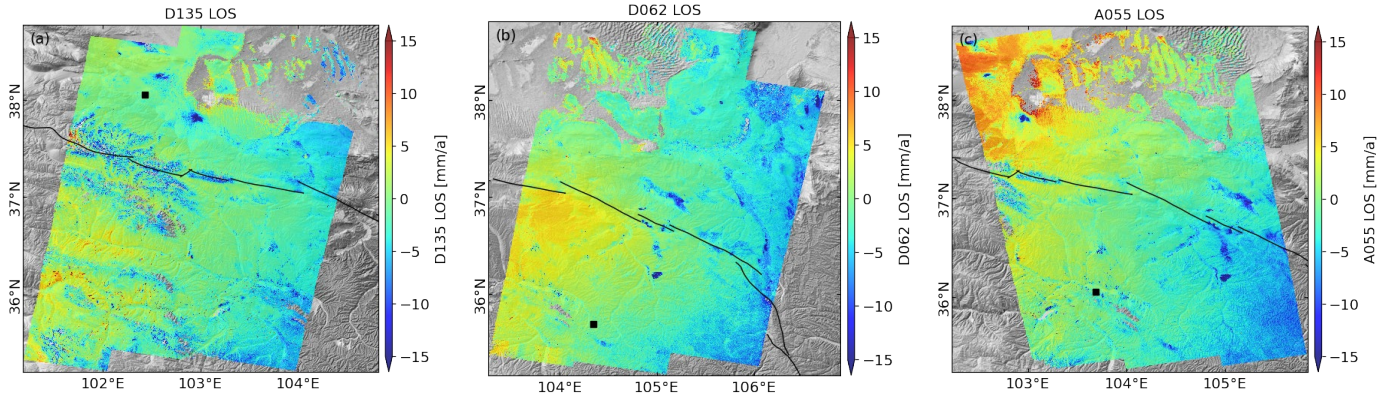


Figure 5. InSAR LOS average velocity for the ascending and descending tracks. (**a**–**c**) represent the LOS velocities of D135, D062, and A055, respectively, with each track relative to a separate reference point (black square). The black lines show the Haiyuan Fault. Positive values indicate that the target moves towards the satellite, whereas negative values indicate that the target moves away from the satellite.

To obtain a consistent velocity across multiple tracks while accounting for long-wavelength signals, such as orbit errors and atmospheric residuals, we tied the InSAR LOS velocity of each track to the Eurasian reference frame adopted by the GNSS velocity [57,58] (Figure 6). The GNSS horizontal velocity with coseismic, postseismic, and seasonal climate effects removed, reflecting stable interseismic tectonic deformation, was derived from Wang and Shen [57]. The GNSS vertical velocity, referenced relative to the Alashan and Ordos blocks to the north, was obtained from Liang et al. [58]. The reference frames for

the GNSS horizontal and vertical velocities were independently defined, but the vertical component exhibited higher noise levels than the horizontal component. Given the dense distribution of GNSS stations in this area, we selectively removed stations that lacked vertical components to ensure data consistency. We adopted the methodology for integrating InSAR and GNSS data described by Hussain et al. [75,76], Weiss et al. [77], and Xu et al. [34]. Initially, we averaged the InSAR velocity of all pixels within a 1 km radius of each GNSS station. Subsequently, we projected the GNSS velocities onto the LOS and computed the difference between the average InSAR and projected GNSS velocities. Using a weighted linear least-square approach, we fitted the residual velocities to determine the best-fitting surface. This fitted surface was then removed from the InSAR LOS velocity, and the InSAR velocities were tied to a fixed Eurasian reference frame, after which any non-tectonic long-wavelength signals (e.g., >100 km) were effectively removed.

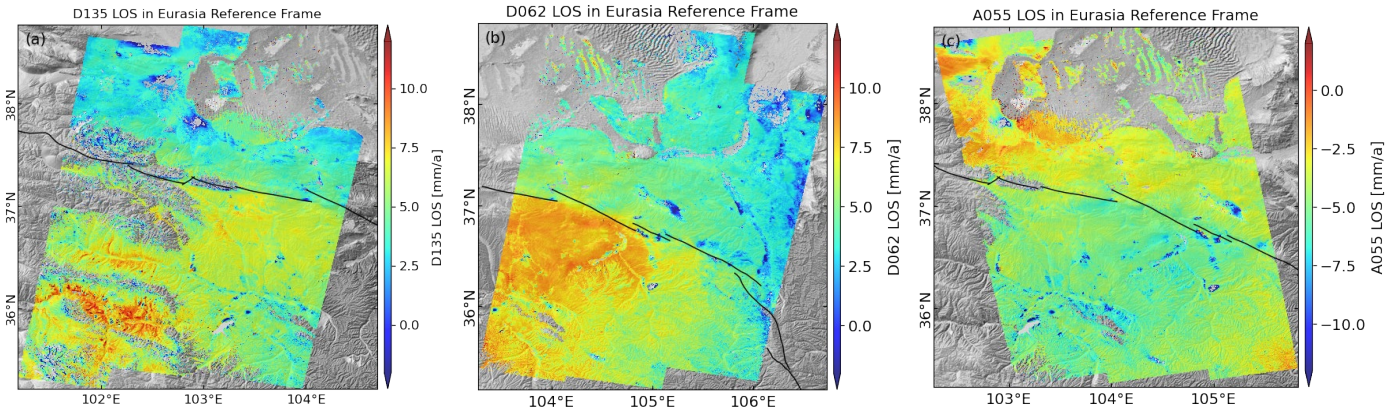


Figure 6. InSAR LOS velocity in the Eurasian reference frame. (**a**–**c**) represent the LOS velocities of D135, D062, and A055, respectively, relative to the fixed Eurasian reference frame. The black lines depict the Haiyuan Fault. Positive values indicate that the target moves towards the satellite, while negative values indicate that the target moves away from the satellite.

3.2. Decomposed Velocity

By interpolation with a spherical model (Equations (4) and (5)), we obtained a smooth north–south velocity (Figure 7), which was then projected onto the LOS of each track to estimate the contribution of north–south movements to the satellite's LOS velocity. We also used an exponential model to fit the parameters of the semivariogram (Figure S3) and found that although there was no significant difference between the two models, the spherical model fit better. The interpolated south–north velocity (Vn) shows good agreement with GNSS measurements (Figure 7). The uncertainties σ(Vn) are primarily controlled by the distribution of GNSS stations, decreasing near the stations and increasing in sparsely instrumented areas. Figure 8 presents the decomposed east–west (Ve) and vertical (Vu) components, and the associated uncertainties (i.e., σ(Ve) and σ(Vu)) are shown in Figure S4. The difference in the Ve map across the fault is more pronounced, and the Vu map shows multiple subsidence centers. From the uncertainty of the Ve and Vu components (Figure S4), it is evident that the uncertainty values for most pixels in the σ(Ve) map are less than 1.5 mm/a, and those in the σ(Vu) map are less than 1 mm/a, indicating that the decomposed velocities are reliable.

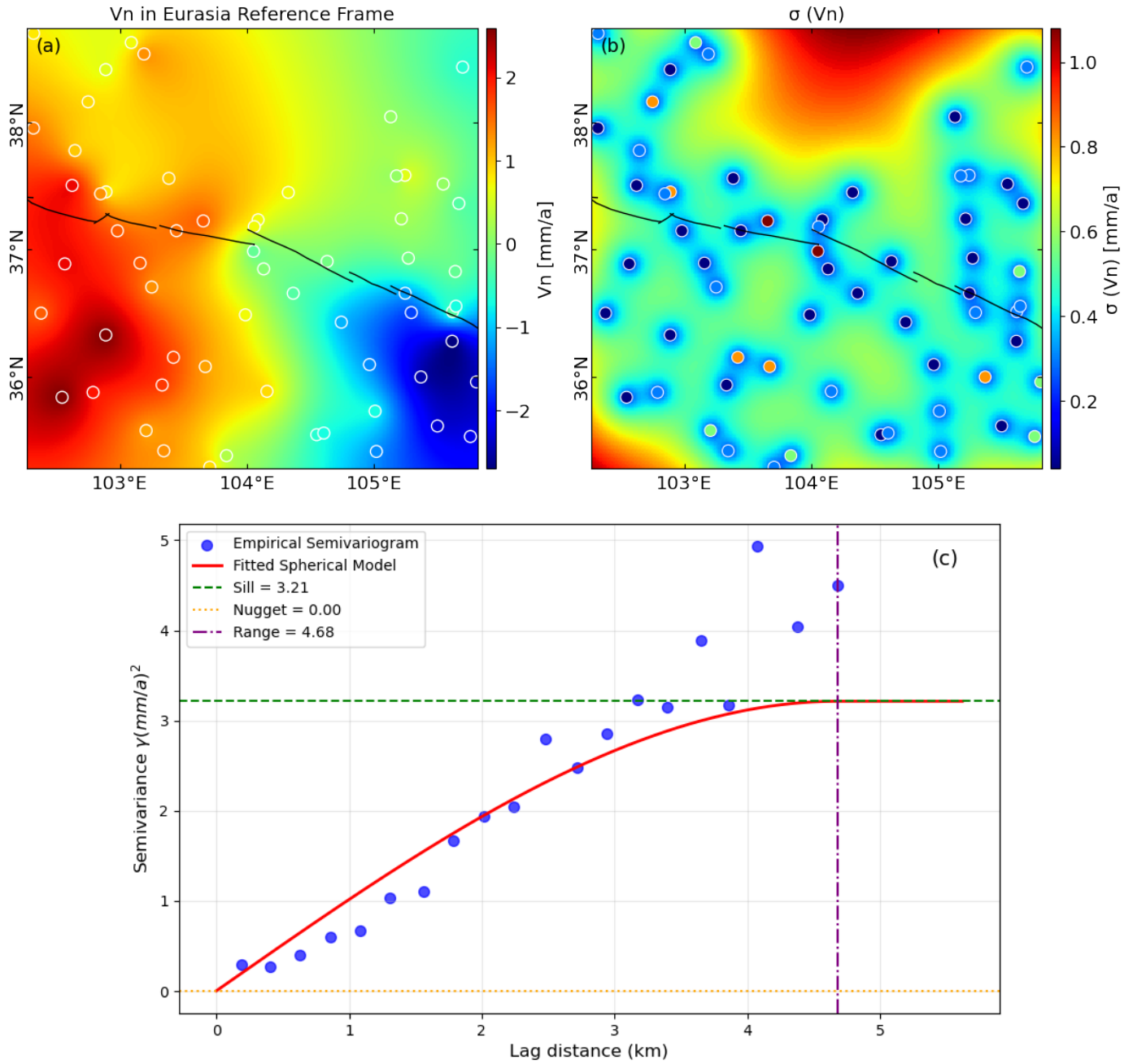


Figure 7. Interpolated (**a**) Vn component and associated uncertainty (**b**) σ(Vn) with a spherical model. The dots with white edge represent GNSS stations from Wang and Shen [57], with color intensity scaled to the magnitudes of Vn in (**a**) and σ(Vn) in (**b**). The black lines show the Haiyuan Fault. Positive (negative) values indicate northward (southward) movement. (**c**) Empirical semivariogram and fitted spherical model. The blue dots and red line indicate the empirical semivariogram and fitted spherical model, respectively. The green, orange, and purple lines correspond to the sill, nugget, and range, respectively.

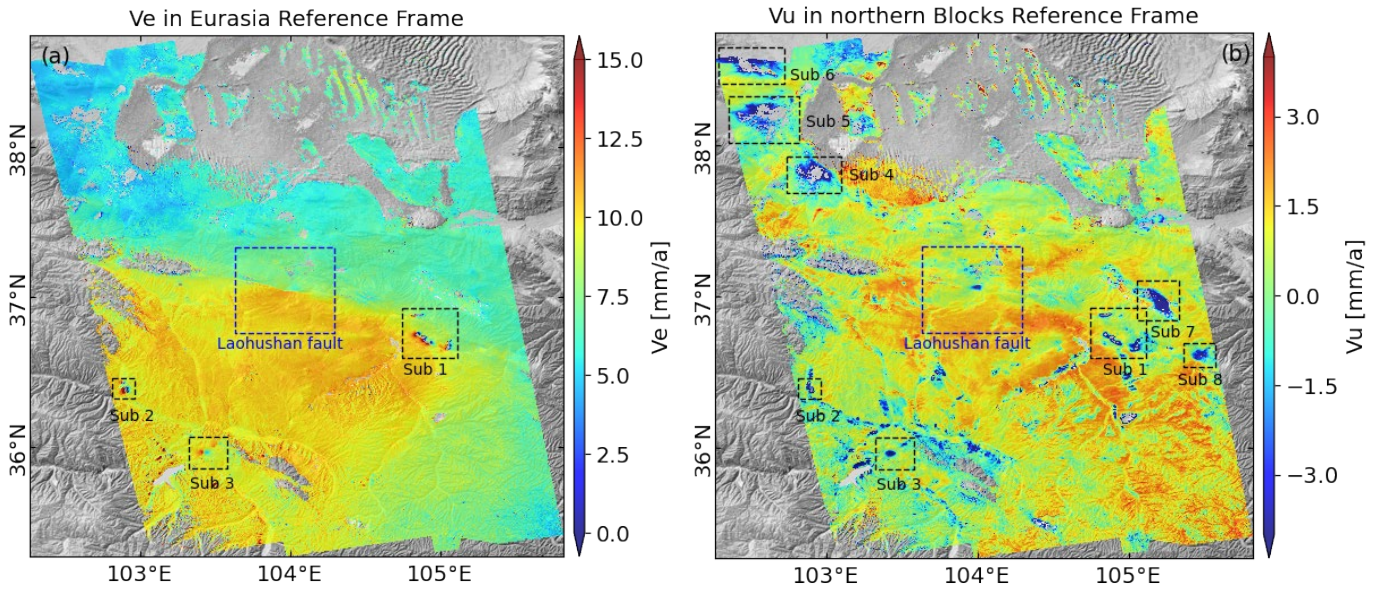


Figure 8. Decomposed (**a**) Ve and (**b**) Vu components. Both the Ve and Vn components are in the fixed Eurasian reference frame [57], while the Vu component is relative to the stable northern block [58]. Positive (negative) values indicate eastward/upward (westward/downward) movement. The dotted polygons (i.e., sub 1 to sub 8) indicate subsidence, which we will discuss in Section 4.1.

Given that the decomposed InSAR and GNSS velocities share the same reference frame, direct comparison between the two measurements is valid. We averaged InSAR pixel values within a 1 km radius of GNSS stations [57,58] and analyzed the InSAR-GNSS relationships (Figures 9 and 10). The fitted regression lines for the Vn and Ve components are "y = 1.00x − 0.02 (R^2 = 0.99)" and "y = 0.93x + 0.52 (R^2 = 0.83)", respectively, indicating strong positive correlations (Figure 9a,c). The histograms of InSAR-GNSS differences reveal mean ± standard deviations of (0.01 ± 0.02 mm/a) for Vn and (−0.03 ± 0.70 mm/a) for Ve (Figure 9b,d), indicating negligible discrepancies. For the Vu component (Figure 9e,f), the linear regression yields "y = 0.33x + 0.37 (R^2 = 0.21)", while its difference histogram shows a mean ± standard deviation of (0.03 ± 0.81 mm/a), with values concentrated within ± 1.5 mm/a of zero. Additionally, the horizontal velocity vectors (i.e., Ve and Vn), derived from the decomposed InSAR Ve and interpolated Vn components, were compared with those of Wang and Shen [57] (Figure 10). As shown in Figures 9 and 10, InSAR and GNSS measurements exhibit a high degree of consistency, suggesting the reliability of the decomposed InSAR results.

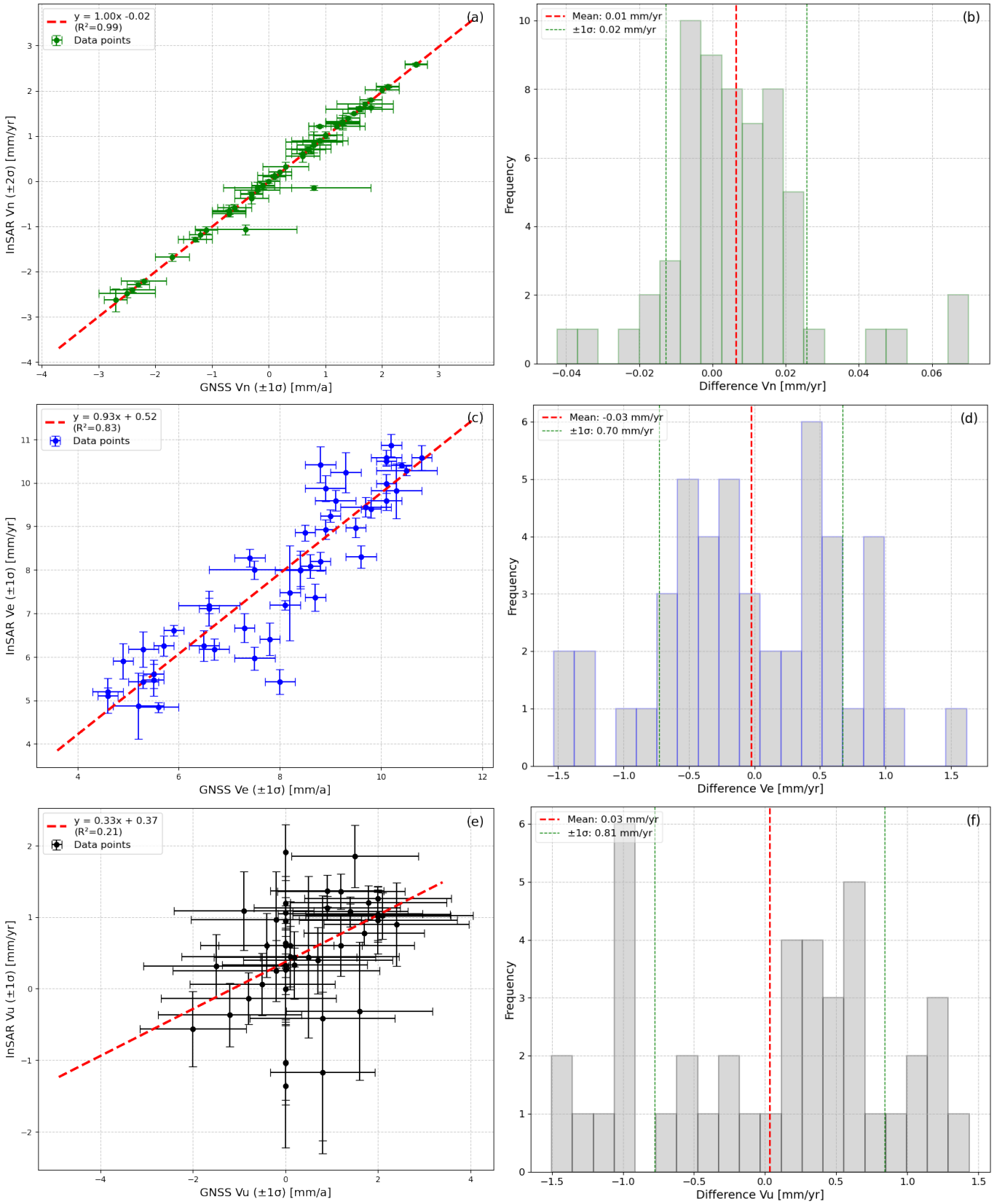


Figure 9. Comparison between InSAR and GNSS measurements. (**a**,**c**,**e**) show scatter plots of the Vn, Ve, and Vu magnitudes with error bars, where red dashed lines indicate fitted regression lines. (**b**,**d**,**f**) present statistical histograms of InSAR-GNSS differences for the Vn, Ve, and Vu components, with red and green dashed lines denoting mean values and standard deviations, respectively.

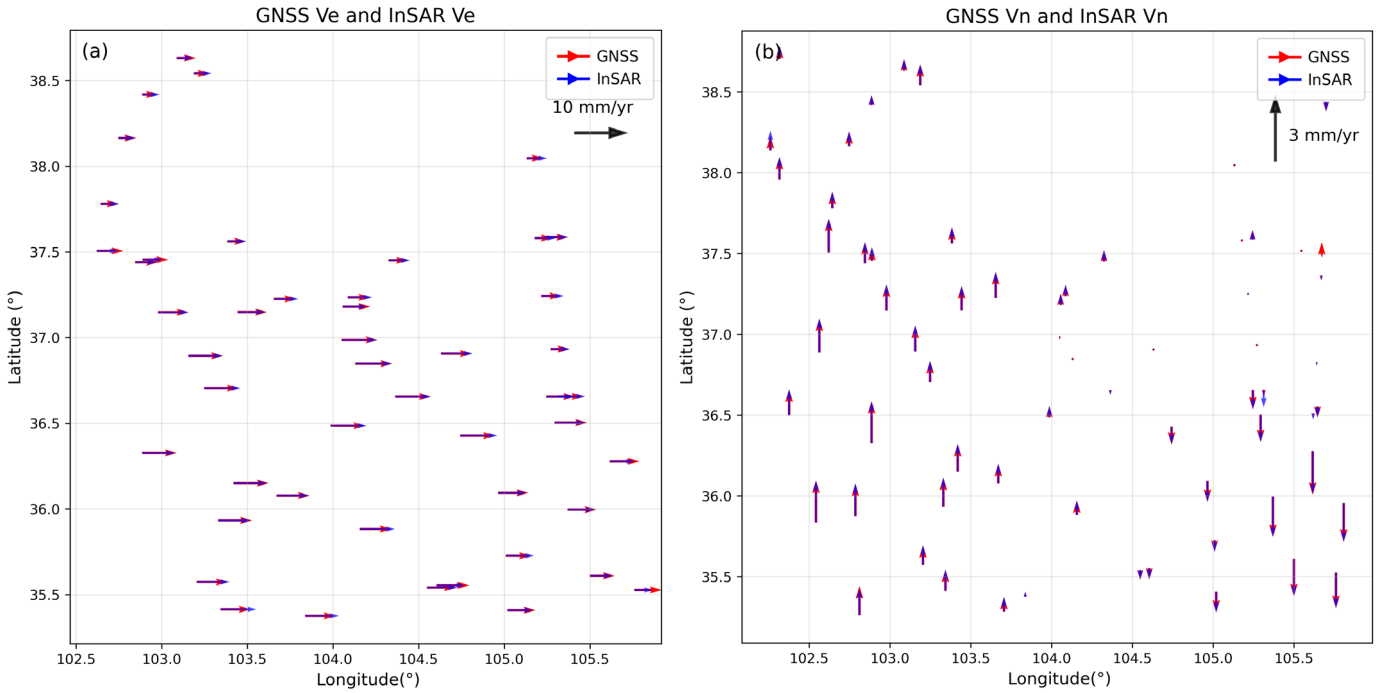


Figure 10. Comparison of horizontal velocity vectors derived from InSAR and GNSS [57]. (**a**,**b**) display the Ve and Vn components, respectively. Note that the scales in (**a**,**b**) are different.

4. Discussion

4.1. Main Features in the Decomposed Velocity

It is evident that a distinct velocity gradient in the east–west component (Ve) was observed along the Haiyuan Fault, reflecting dominant strike–slip motion. Noting that a sharp gradient variation extending ~45 km exists along the strike of the Laohushan segment, suggesting that shallow creep [43–45] has propagated to the surface (Figure 11a). The differential movement across the fault is approximately 3 mm/a from the profile (Figure 11b). This cross-fault discontinuous velocity is superimposed on a velocity with longer wavelength and smoother variation. However, the severe incoherence of the velocity in the Maomaoshan segment to the west prevents us from determining whether a velocity discontinuity exists (Figure 8). Although Li et al. [50] found two shallow creep sections along the surface rupture zone of the 1920 Haiyuan earthquake, our east–west velocity component did not exhibit an abrupt discontinuity (Figure 8), suggesting that aseismic slip may not have reached the surface. The vertical velocity component (Vu) does not show discontinuity across the fault, indicating that the fault movement is mainly along the fault strike. According to the Vu, there is a significant subsidence signal in the Jingtai Basin (Figure 11c), with a subsidence center with a maximum value of approximately −6 mm/a (Figure 11d). It is obvious that the subsidence variation is continuous from the profile, which may be caused by compaction of unconsolidated sediments or groundwater extraction. Moreover, the Jingtai Basin is located in a pull-apart basin between the Laohushan fault to the west and the rupture zone of the 1920 Haiyuan Mw7.9 earthquake to the east. Therefore, slow tectonic movements cannot be ruled out as contributing factors to subsidence. On the east side of the rupture zone, we also identified two subsidence centers with maximum subsidence rates of −12 mm/a and −6 mm/a, respectively (Figure S5). We attribute this continuous variation primarily to human activities, such as groundwater extraction.

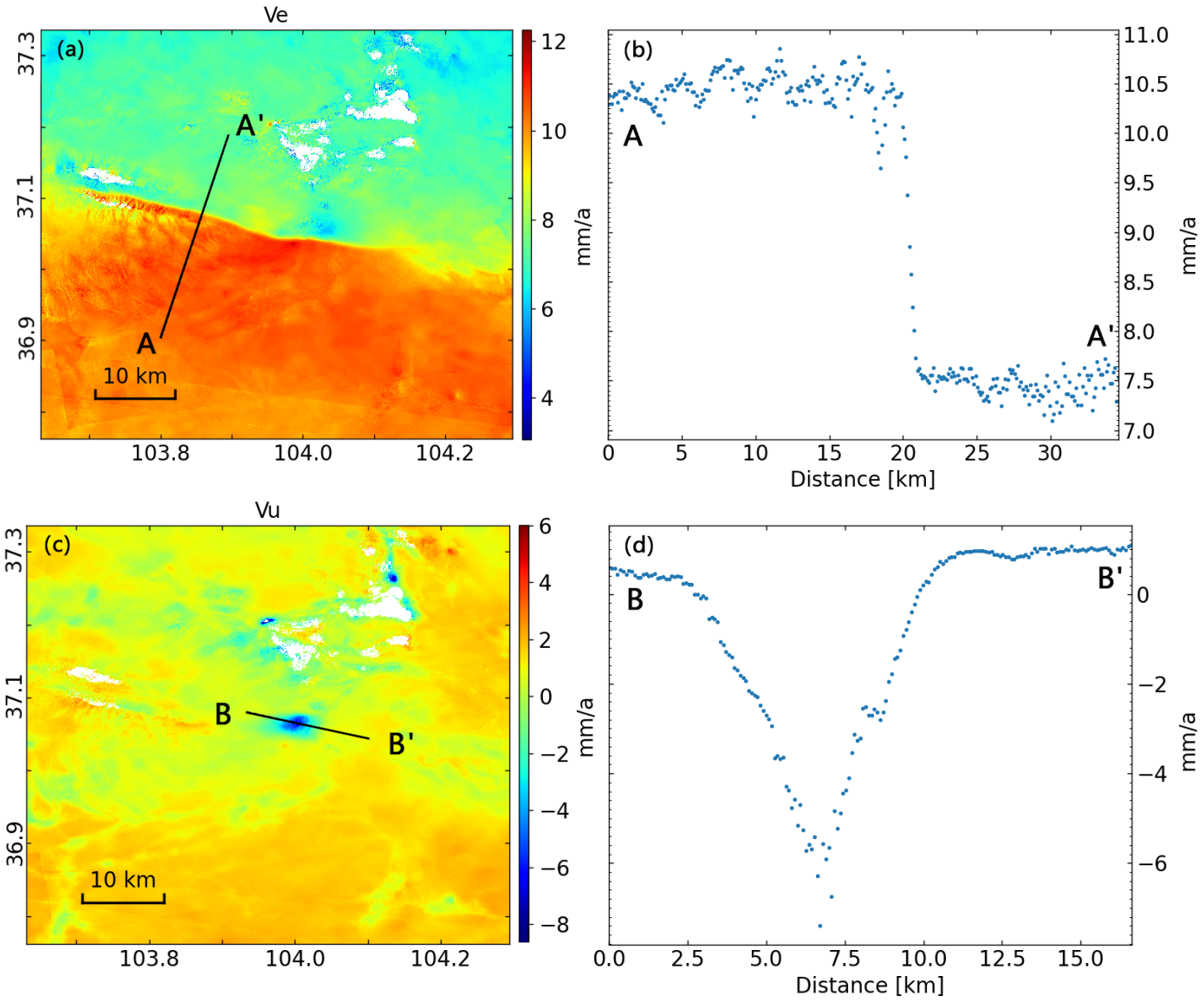


Figure 11. Enlarged views across the Laohushan segment of the Haiyuan Fault. (**a**) indicates the Laohushan fault in the Ve component, and (**c**) shows the Jingtai Basin in the Vu component. (**b**) Profile AA′ is perpendicular to the Laohushan fault, while (**d**) profile BB′ crosses the Jingtai Basin subsidence center.

Our results reveal several notable phenomena. Significant lateral variations in the Ve component coincide with subsidence signals in the Vu component (Figure 12). The deformation field exhibits data voids within the subsidence center owing to severe decorrelation, which was attributed to coal mining [54]. Additionally, multiple areas show negligible Ve deformation but pronounced subsidence in the Vu map, displaying arcuate deformation features (Figures 13 and S6). The central data voids within these features, resulting from intense decorrelation, are consistent with hydrologically driven deformation mechanisms, such as lake dynamics.

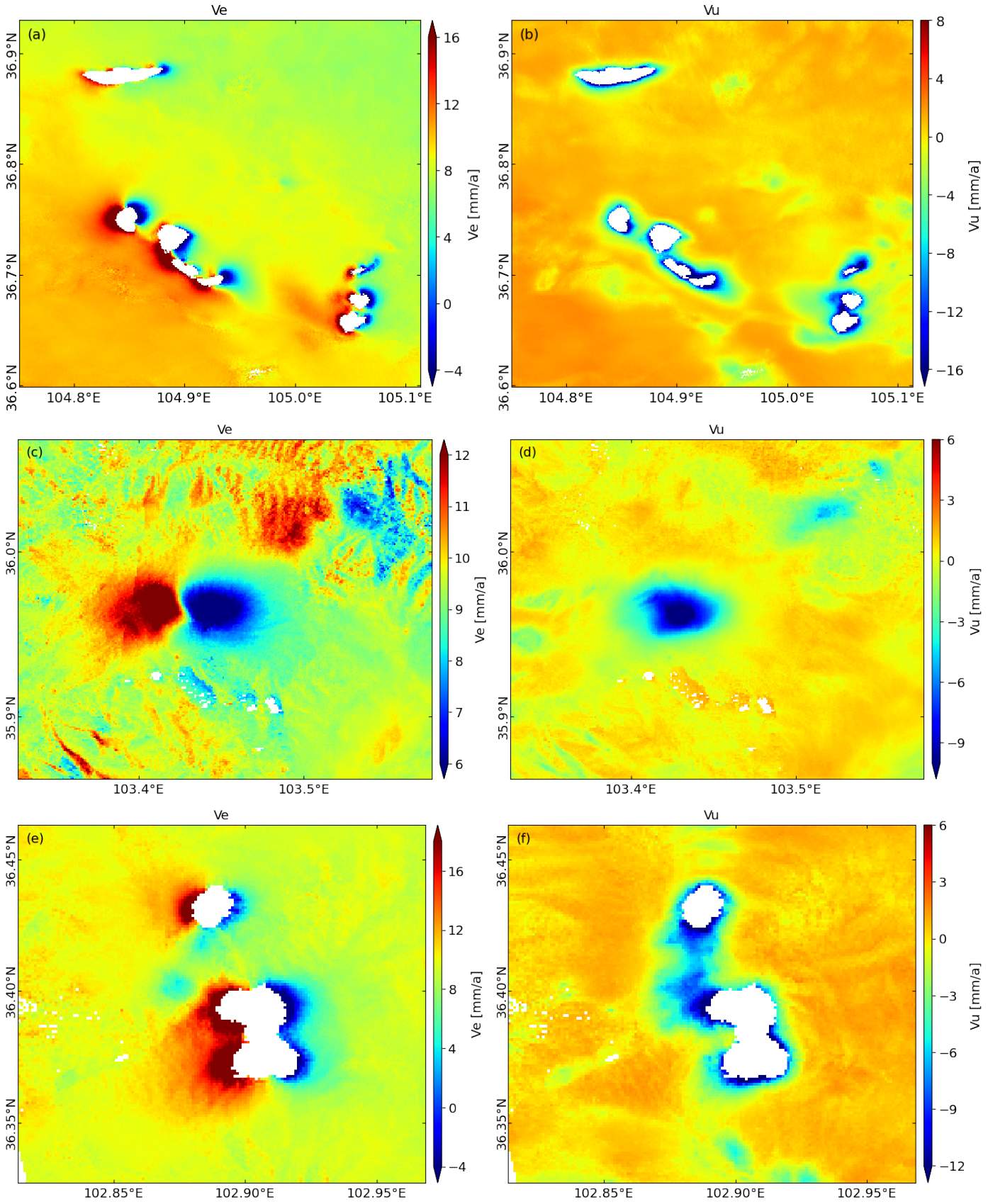


Figure 12. Enlarged views of (**a**) subsidence 1, (**c**) subsidence 2, and (**e**) subsidence 3 in the Ve component, and (**b**,**d**,**f**) in the Vu component.

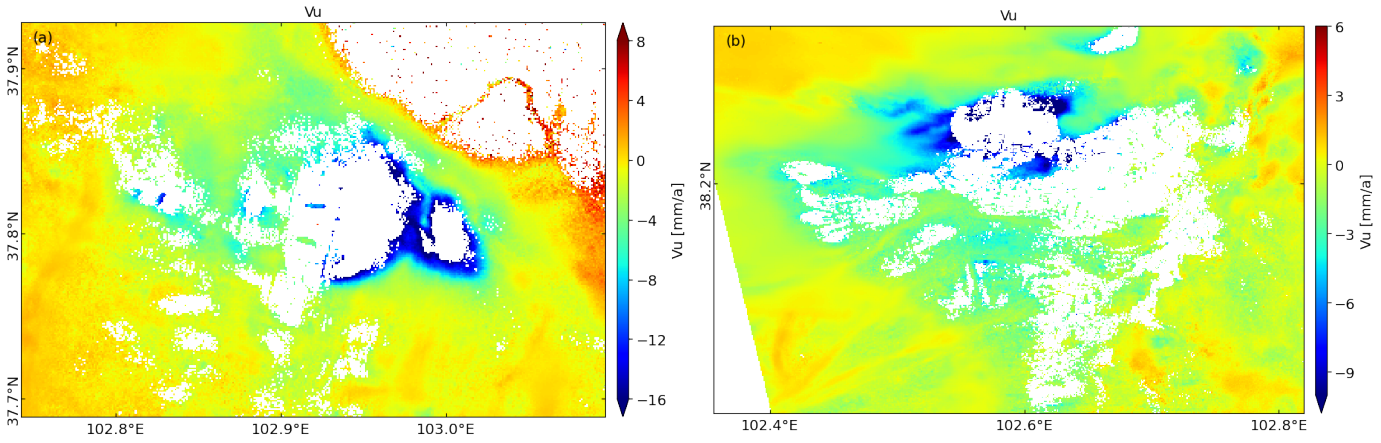


Figure 13. Enlarged views of (**a**) subsidence 4 and (**b**) subsidence 5 in the Vu component.

4.2. Uncertainty of the Decomposed Velocity

Our InSAR-GNSS integration method resembles those of Hussain et al. [75,76] and Weiss et al. [77]; both studies successfully investigated the North Anatolian Fault. However, they only utilized GNSS horizontal velocities for reference frame tying, assuming negligible vertical motion, which may inevitably overestimate or underestimate the InSAR velocity. Owing to the dense distribution of GNSS stations and high-precision observations, we comprehensively utilized GNSS horizontal and vertical velocities to tie the InSAR velocity to the Eurasian reference frame. Additionally, Wei et al. [11], Tong et al. [12], and Xu et al. [34] used the "Remove/Filter/Restore" approach for data fusion of InSAR and GNSS to study the San Andreas Fault deformation. The method involved removing the GNSS measurements projected into the LOS direction from the stacked InSAR velocity, filtering the residual stack to further address orbital and atmospheric errors, and adding the GNSS measurements back to the filtered stack to restore the full LOS velocity. We estimated the errors of the residual phase through quadratic polynomial fitting instead of filtering, yet both methods are aimed at mitigating long-wavelength non-tectonic signals. Previous studies have demonstrated 3D deformation on the northeastern Tibetan Plateau [52,54–56]. However, Wu et al. [52] tied InSAR velocities to the Ordos reference frame, making them incomparable with our Eurasian reference frame results. Liu et al. [55,56] obtained large-scale, kilometer-resolution 3D velocity fields with smoother results that failed to capture smaller-scale deformation signals. Our decomposed velocity, which showed good agreement with Ou et al. [54] in identical study regions, can distinguish deformation with distinct characteristics caused by different factors, such as hydrological and anthropogenic processes.

Owing to the near-polar orbit flight and side-looking imaging of radar satellites, InSAR is most sensitive to vertical ground movements but insensitive to movements in the north–south direction. Assuming that ground movements in the north–south direction can be neglected, this is reasonable for near-east–west strike–slip faults [74]. Nevertheless, given the N110°E strike of the Haiyuan Fault, neglecting north–south component would introduce significant errors. The uncertainties of most pixels in our decomposed Ve and Vu velocity fields are below 1 mm/a, with maximum uncertainties for Ve and Vu being less than 2 mm/a and 1.5 mm/a, respectively, indicating the reliability of the decomposed velocities. In light of the high precision of GNSS Ve observations, the strong positive correlation between InSAR-derived Ve and GNSS Ve demonstrates the rationality and effectiveness of tying the InSAR LOS velocity to the fixed Eurasian reference frame. However, InSAR Vu and GNSS Vu exhibited a weaker positive correlation. This fit is not surprising, considering that the uncertainties associated with GNSS Vu are almost as large as their absolute values.

Owing to the small incidence angle of radar satellites, InSAR exhibits greater sensitivity and higher precision for vertical displacements than for horizontal components. Nonetheless, the differences between InSAR Vu and GNSS Vu are concentrated within a distribution characterized by a mean ± standard deviation of (0.03 ± 0.81 mm/a), suggesting that the discrepancies are minor. Moreover, the observation periods of the InSAR and GNSS data are not entirely identical, and a single observation may not necessarily capture the changes in deformation. Overall, the horizontal deformation rates have remained relatively stable over the past three decades [5,57,58,62,63]. However, vertical deformation is highly complex and susceptible to influences from anthropogenic activities, hydrological conditions, and variations in surface mass loading [79–82]. Consequently, vertical deformation within a 1 km radius of the GNSS station may also undergo changes, potentially leading to discrepancies between the averaged InSAR vertical velocity and GNSS measurements.

5. Conclusions

In this study, we investigated the 3D surface deformation across the Laohushan section and the Haiyuan earthquake rupture zone of the Haiyuan Fault. First, we provided a detailed description of the geometric relationship between satellite observations and the 3D surface deformation. Subsequently, we aligned the InSAR velocities with the stable Eurasian reference frame adopted by GNSS to achieve consistent results, so that the InSAR and GNSS data could be directly compared. Under the constraint of the south–north component of GNSS with Kriging interpolation, InSAR velocities were then decomposed into east–west and vertical velocities, which can accurately reflect true surface deformation. We found that a sharp velocity gradient extending ~45 km along the strike of the Laohushan segment, with a differential movement of ~3 mm/a across the fault, was observed in the east–west velocity component, suggesting that shallow creep has propagated to the surface. However, the east–west velocity component did not exhibit an abrupt discontinuity in the rupture zone of the Haiyuan earthquake. Therefore, it is necessary to further investigate the kinematic parameters of faults by jointly constraining parameter inversion from the InSAR and GNSS data. We also found several subsidence centers in the vertical velocity component, such as the Jingtai Basin. Subsidence caused by anthropogenic and hydrological processes in the region, such as groundwater extraction, coal mining, and hydrologic effects, exhibited distinct distribution characteristics in the vertical velocity component.

Supplementary Materials: The following supporting information can be downloaded at https://www.mdpi.com/article/10.3390/rs18010142/s1, Figure S1: InSAR time-perpendicular baseline; Figure S2: The mosaic velocity of descending tracks D135 and D062; Figure S3: Interpolated Vn and associated uncertainty σ(Vn) with an exponential model; Figure S4: Uncertainties of the decomposed Ve and Vu components; Figure S5: Enlarged views of subsidence 7 and subsidence 8 in the Vu component; Figure S6: Enlarged view of subsidence 6 in the Vu component.

Author Contributions: Conceptualization, X.W. and Y.S.; methodology, X.W.; software, X.W.; validation, X.W., M.L. and Z.Y.; formal analysis, X.W. and M.L.; investigation, X.W. and L.L.; resources, Y.S.; data curation, X.W.; writing—original draft preparation, X.W.; writing—review and editing, X.W. and M.L.; visualization, X.W. and Z.Y.; supervision, Y.S.; project administration, M.L. and X.B.; funding acquisition, Y.S. All authors have read and agreed to the published version of the manuscript.

Funding: This research was funded by the Construction of the Provincial Key Laboratory for Microwave Spatial Intelligent Cloud Computing, grant number 2025ZY01019, and the Project of Microwave Scattering Properties Measurement System, Remote Sensing Experiment and Evaluation Platform, grant number E23Z05020D.

Data Availability Statement: The ascending and descending Sentinel-1 SAR images were open accessed from the Alaska SAR Facility (ASF, https://search.asf.alaska.edu/ (accessed on 1 November

2024)). GNSS velocities were derived from Wang and Shen [57] and Liang et al. [58]. The fault traces data were derived from the National Earthquake Data Center (http://data.earthquake.cn (accessed on 5 November 2024)). The SAR images were processed by ISCE2 (version 2.6.1) [65,66] and Mintpy (version 1.6.1) [68]. Some figures were generated by the Generic Mapping Tools (version 6.4.0) [64].

Acknowledgments: We thank Falk Amelung and Weijun Gan for insightful discussions. We appreciate the constructive comments and advices from the editors and six anonymous reviewers.

Conflicts of Interest: The authors declare no conflicts of interest.

References

1. Wright, T.J.; Elliott, J.R.; Wang, H.; Ryder, I. Earthquake cycle deformation and the moho: Implications for the rheology of continental lithosphere. *Tectonophysics* **2013**, *609*, 504–523. [CrossRef]
2. Avouac, J.P. From geodetic imaging of seismic and aseismic fault slip to dynamic modeling of the seismic cycle. *Annu. Rev. Earth Planet. Sci.* **2015**, *43*, 233–271. [CrossRef]
3. Elliott, J.R.; Walters, R.J.; Wright, T.J. The role of space-based observation in understanding and responding to active tectonics and earthquakes. *Nat. Commun.* **2016**, *7*, 13844. [CrossRef]
4. Bürgmann, R.; Thatcher, W. Space geodesy: A revolution in crustal deformation measurements of tectonic processes. In *The Web of Geological Sciences: Advances, Impacts, and Interactions*; Bickford, M.E., Ed.; Geological Society of America: Boulder, CO, USA, 2013; pp. 397–430. [CrossRef]
5. Wang, Q.; Zhang, P.Z.; Freymueller, J.T.; Bilham, R.; Larson, K.M.; Lai, X.; You, X.; Niu, Z.; Wu, J.; Li, Y.; et al. Present-day crustal deformation in China constrained by global positioning system measurements. *Science* **2001**, *294*, 574–577. [CrossRef]
6. Berardino, P.; Fornaro, G.; Lanari, R.; Sansosti, E. A new algorithm for surface deformation monitoring based on small baseline differential SAR interferograms. *IEEE Trans. Geosci. Remote Sens.* **2002**, *40*, 2375–2383. [CrossRef]
7. Ferretti, A.; Prati, C.; Rocca, F. Permanent scatterers in SAR interferometry. *IEEE Trans. Geosci. Remote Sens.* **2001**, *39*, 8–20. [CrossRef]
8. Hooper, A.; Bekaert, D.; Spaans, K.; Arkan, M. Recent advances in SAR interferometry time series analysis for measuring crustal deformation. *Tectonophysics* **2012**, *514–517*, 1–13. [CrossRef]
9. Biggs, J.; Wright, T.J. How satellite InSAR has grown from opportunistic science to routine monitoring over the last decade. *Nat. Commun.* **2020**, *11*, 3863. [CrossRef]
10. Li, S.; Xu, W.; Li, Z. Review of the SBAS InSAR Time-series algorithms, applications, and challenges. *Geodes. Geodyn.* **2022**, *13*, 114–126. [CrossRef]
11. Wei, M.; Sandwell, D.; Smith-Konter, B. Optimal combination of InSAR and GPS for measuring interseismic crustal deformation. *Adv. Space Res.* **2010**, *46*, 236–249. [CrossRef]
12. Tong, X.; Sandwell, D.T.; Smith-Konter, B. High-resolution interseismic velocity data along the San Andreas Fault from GPS and InSAR. *J. Geophys. Res. Solid. Earth* **2013**, *118*, 369–389. [CrossRef]
13. Fialko, Y.; Sandwell, D.; Simons, M.; Rosen, P. Three-dimensional deformation caused by the Bam, Iran, earthquake and the origin of shallow slip deficit. *Nature* **2005**, *435*, 295–299. [CrossRef]
14. Fattahi, H.; Amelung, F. InSAR observations of strain accumulation andfault creep along the Chaman Fault system, Pakistan and Afghanistan. *Geophys. Res. Lett.* **2016**, *43*, 8399–8406. [CrossRef]
15. Zhao, B.; Bürgmann, R.; Wang, D.; Zhang, J.; Yu, J.; Li, Q. Aseismic slip and recent ruptures of persistent asperities along the Alaska-Aleutian subduction zone. *Nat. Commun.* **2022**, *13*, 3098. [CrossRef]
16. Farquharson, J.I.; Amelung, F. Extreme rainfall triggered the 2018 rift eruption at Kīlauea Volcano. *Nature* **2020**, *580*, 491–495. [CrossRef] [PubMed]
17. Hilley, G.E.; Burgmann, R.; Ferretti, A.; Novali, F.; Rocca, F. Dynamics of Slow-Moving Landslides from Permanent Scatterer Analysis. *Science* **2004**, *304*, 1952−1955. [CrossRef] [PubMed]
18. Argus, D.F.; Gordon, R.G.; Heflin, M.B.; Ma, C.; Eanes, R.J.; Willis, P.; Peltier, W.R.; Owen, S.E. The angular velocities of the plates and the velocity of Earth's centre from space geodesy. *Geophys. J. Int.* **2010**, *180*, 913–960. [CrossRef]
19. Altamimi, Z.; Rebischung, P.; Métivier, L.; Collilieux, X. ITRF 2014: A new release of the International Terrestrial Reference Frame modeling nonlinear station motions. *J. Geophys. Res. Solid Earth* **2016**, *121*, 6109–6131. [CrossRef]
20. Kreemer, C.; Blewitt, G.; Klein, E.C. A geodetic plate motion and global strain rate model. *Geochem. Geophys. Geosyst.* **2014**, *15*, 3849–3889. [CrossRef]
21. Li, Z.; Zhao, R.; Hu, J.; Wen, L.; Feng, G.; Zhang, Z.; Wang, Q. InSAR analysis of surface deformation over permafrost to estimate active layer thickness based on one-dimensional heat transfer model of soils. *Sci. Rep.* **2015**, *5*, 15542. [CrossRef]
22. Daout, S.; Doin, M.P.; Peltzer, G.; Socquet, A.; Lasserre, C. Large-scale InSAR monitoring of permafrost freeze-thaw cycles on the Tibetan Plateau. *Geophys. Res. Lett.* **2017**, *44*, 901–909. [CrossRef]

23. Chaussard, E.; Wdowinski, S.; Cabral-Cano, E.; Amelung, F. Land subsidence in central Mexico detected by ALOS InSAR time-series. *Remote Sens. Environ.* **2014**, *140*, 94–106. [CrossRef]
24. Buzzanga, B.; Bekaert, D.P.S.; Hamlington, B.D.; Sangha, S.S. Toward sustained monitoring of subsidence at the coast using InSAR and GPS: An application in Hampton Roads, Virginia. *Geophys. Res. Lett.* **2020**, *47*, e2020GL090013. [CrossRef]
25. Liu, Y.; Liu, J.; Xia, X.; Bi, H.; Huang, H.; Ding, R.; Zhao, L. Land subsidence of the Yellow River Delta in China driven by river sediment compaction. *Sci. Total Environ.* **2021**, *750*, 142165. [CrossRef]
26. He, Z.; Yang, Z.; Wu, X.; Zhang, T.; Song, M.; Liu, M. Triggering of Land Subsidence in and Surrounding the Hangjiahu Plain Based on Interferometric Synthetic Aperture Radar Monitoring. *Remote Sens.* **2024**, *16*, 1864. [CrossRef]
27. Ao, Z.; Hu, X.; Tao, S.; Hu, X.; Wang, G.; Li, M.; Wang, F.; Hu, L.; Liang, X.; Xiao, J.; et al. A national-scale assessment of land subsidence in China's major cities. *Science* **2024**, *384*, 301–306. [CrossRef]
28. Hanssen, R.F. *Radar Interferometry: Data Interpretation and Error Analysis*; Kluwer Academic Publishers: Dordrecht, The Netherlands, 2001.
29. Wright, T.J.; Parsons, B.E.; Lu, Z. Toward mapping surface deformation in three dimensions using InSAR. *Geophys. Res. Lett.* **2004**, *31*, L01607. [CrossRef]
30. Neely, W.R.; Borsa, A.A.; Silverii, F. GInSAR: A cGPS Correction for Enhanced InSAR Time Series. *IEEE Trans. Geosci. Remote Sens.* **2019**, *58*, 136–146. [CrossRef]
31. Wang, H.; Wright, T.J.; Liu-Zeng, J.; Peng, L. Strain rate distribution in south-central Tibet from two decades of InSAR and GPS. *Geophys. Res. Lett.* **2019**, *46*, 5170–5179. [CrossRef]
32. Farolfi, G.; Bianchini, S.; Casagli, N. Integration of GNSS and Satellite InSAR Data: Derivation of Fine-Scale Vertical Surface Motion Maps of Po Plain, Northern Apennines, and Southern Alps, Italy. *IEEE Trans. Geosci. Remote Sens.* **2018**, *57*, 319–328. [CrossRef]
33. Gudmundsson, S.; Sigmundsson, F.; Carstensen, J.M. Three-dimensional surface motion maps estimated from combined interferometric synthetic aperture radar and GPS data. *J. Geophys. Res.* **2002**, *107*, 2250. [CrossRef]
34. Xu, X.; Sandwell, D.T.; Klein, E.; Bock, Y. Integrated Sentinel-1 InSAR and GNSS time-series along the San Andreas fault system. *J. Geophys. Res. Solid. Earth* **2021**, *126*, e2021JB022579. [CrossRef]
35. Hu, J.; Li, Z.W.; Ding, X.L.; Zhu, J.J.; Sun, Q. Derivation of 3-D coseismic surface displacement fields for the 2011 Mw 9.0 Tohoku-Oki earthquake from InSAR and GPS measurements. *Geophys. J. Int.* **2013**, *192*, 573–585. [CrossRef]
36. Hu, J.; Li, Z.W.; Ding, X.L.; Zhu, J.J.; Zhang, L.; Sun, Q. Resolving three-dimensional surface displacements from InSAR measurements: A review. *Earth-Sci. Rev.* **2014**, *133*, 1–17. [CrossRef]
37. Guo, N.; Zhan, W. Influence of different data fusion methods on the accuracy of three-dimensional displacements field. *Adv. Space Res.* **2020**, *65*, 1580–1590. [CrossRef]
38. Shen, Z.K.; Liu, Z. Integration of GPS and InSAR data for resolving 3-dimensional crustal deformation. *Earth Space Sci.* **2020**, *7*, e2019EA001036. [CrossRef]
39. Xu, K.; Gan, W.; Wu, J.; Hou, Z. A robust method for 3-D surface displacement fields combining GNSS and single-orbit InSAR measurements with directional constraint from elasticity model. *GPS Solut.* **2022**, *26*, 46. [CrossRef]
40. Liu, J.; Xu, J.; Ou, Q.; Han, L.F.; Wang, Z.J.; Shao, Z.G.; Zhang, P.Z.; Yao, W.Q.; Wang, P. Discussion on the overestimated magnitude of the 1920 Haiyuan earthquake. *Acta Seismol. Sin.* **2023**, *45*, 579–596. (In Chinese) [CrossRef]
41. Yuan, D.; Ge, W.; Chen, Z.; Li, C.; Wang, Z.; Zhang, H.; Zhang, P.; Zheng, D.; Zheng, W.; Craddock, W.H.; et al. The growth of northeastern Tibet and its relevance to large-scale continental geodynamics: A review of recent studies. *Tectonics* **2013**, *32*, 1358–1370. [CrossRef]
42. Zheng, W.; Zhang, P.; He, W.; Yuan, D.; Shao, Y.; Zheng, D.; Ge, W.; Min, W. Transformation of displacement between strike-slip and crustal shortening in the northern margin of the Tibetan Plateau: Evidence from decadal GPS measurements and late Quaternary slip rates on faults. *Tectonophysics* **2013**, *584*, 267–280. [CrossRef]
43. Cavalié, O.; Lasserre, C.; Doin, M.P.; Peltzer, G.; Sun, J.; Xu, X.; Shen, Z.K. Measurement of interseismic strain across the Haiyuan fault (Gansu, China), by InSAR. *Earth Planet. Sci. Lett.* **2008**, *275*, 246–257. [CrossRef]
44. Jolivet, R.; Lasserre, C.; Doin, M.P.; Guillaso, S.; Peltzer, G.; Dailu, R.; Sun, J.; Shen, Z.K.; Xu, X. Shallow creep on the Haiyuan Fault (Gansu, China) revealed by SAR Interferometry. *J. Geophys. Res. Solid. Earth* **2012**, *117*, B06401. [CrossRef]
45. Jolivet, R.; Lasserre, C.; Doin, M.P.; Peltzer, G.; Avouac, J.P.; Sun, J.; Dailu, R. Spatio-temporal evolution of aseismic slip along the Haiyuan Fault, China: Implications for fault frictional properties. *Earth Planet. Sci. Lett.* **2013**, *377–378*, 23–33. [CrossRef]
46. Daout, S.; Jolivet, R.; Lasserre, C.; Doin, M.P.; Barbot, S.; Tapponnier, P.; Peltzer, G.; Socquet, A.; Sun, J. Along-strike variations of the partitioning of convergence across the Haiyuan fault system detected by InSAR. *Geophys. J. Int.* **2016**, *205*, 536–547. [CrossRef]
47. Huang, Z.; Zhou, Y.; Qiao, X.; Zhang, P.; Cheng, X. Kinematics of the ~1000 km Haiyuan Fault system in northeastern Tibetan Plateau from high-resolution Sentinel-1 InSAR velocities: Fault architecture, slip rates, and partitioning. *Earth Planet. Sci. Lett.* **2022**, *583*, 117450. [CrossRef]

48. Wu, X.; Liu, M.; Shao, Y.; Gan, W.; Yang, Z.; He, Z.; Bian, X.; Zhang, T.; Xie, C. Variations in slip rate along the Haiyuan Fault Zone based on geological and geodetic estimations: Implications for strain accumulation and seismic hazard. *Big Earth Data* **2024**, *8*, 587–607. [CrossRef]
49. Zhang, K.; Gan, W.; Liang, S.; Xiao, G.; Dai, C.; Liu, Z.; Zhang, L. Shallow creep on the Laohushan Segment of the Haiyuan fault, northeastern Tibetan plateau, detected with dense near-field GPS measurements. *Geophys. Res. Lett.* **2024**, *51*, e2024GL108764. [CrossRef]
50. Li, Y.; Nocquet, J.M.; Shan, X.; Song, X. Geodetic observations of shallow creep on the Laohushan-Haiyuan fault, northeastern Tibet. *J. Geophys. Res. Solid Earth* **2021**, *126*, e2020JB021576. [CrossRef]
51. Guo, N.; Wu, Y.; Su, G. Analysis of the fault slip, creep, and coupling characteristics of the Maomaoshan-Laohushan-Haiyuan Fault using InSAR and GNSS measurements. *Tectonophysics* **2023**, *863*, 229988. [CrossRef]
52. Wu, D.; Ge, W.; Liu, S.; Yuan, D.; Zhang, B.; Wei, C. Present-day 3D crustal deformation of the northeastern Tibetan Plateau from space geodesy. *Geophys. Res. Lett.* **2024**, *51*, e2023GL106143. [CrossRef]
53. Jiang, F.; Ji, L.; Liu, C.; Zhu, L.; Liu, L.; Xu, J. Persistent postseismic signals: Multigeodetic insights into the 1920 Haiyuan earthquake's legacy. *Tectonophysics* **2025**, *912*, 230856. [CrossRef]
54. Ou, Q.; Daout, S.; Weiss, J.R.; Shen, L.; Lazecký, M.; Wright, T.J.; Parsons, B.E. Large-scale interseismic strain mapping of the NE Tibetan Plateau from Sentinel-1 interferometry. *J. Geophys. Res. Solid Earth* **2022**, *127*, e2022JB024176. [CrossRef]
55. Liu, C.; Ji, L.; Zhu, L.; Xu, C.; Zhang, W.; Qiu, J.; Xiong, G. Present-Day Three-Dimensional Deformation across the Ordos Block, China, Derived from InSAR, GPS, and Leveling Observations. *Remote Sens.* **2023**, *15*, 2890. [CrossRef]
56. Liu, C.; Ji, L.; Zhu, L.; Xu, C.; Zhao, C.; Lu, Z.; Wang, Q. Kilometer-resolution three-dimensional crustal deformation of Tibetan Plateau from InSAR and GNSS. *Sci. China Earth Sci.* **2024**, *67*, 1818–1835. [CrossRef]
57. Wang, M.; Shen, Z.K. Present-day crustal deformation of continental China derived from GPS and its tectonic implications. *J. Geophys. Res. Solid Earth* **2020**, *125*, e2019JB018774. [CrossRef]
58. Liang, S.; Gan, W.; Shen, C.; Xiao, G.; Liu, J.; Chen, W.; Ding, X.; Zhou, D. Three-dimensional velocity field of present-day crustal motion of the Tibetan Plateau derived from GPS measurements. *J. Geophys. Res. Solid. Earth* **2013**, *118*, 5722–5732. [CrossRef]
59. Farr, T.G.; Rosen, P.A.; Caro, E.; Crippen, R.; Duren, R.; Hensley, S.; Kobrick, M.; Paller, M.; Rodriguez, E.; Roth, L.; et al. The shuttle radar topography mission. *Rev. Geophys.* **2007**, *45*, RG2004. [CrossRef]
60. Taylor, M.; Yi, A. Active structures of the Himalayan-Tibetan orogen and their relationships to earthquake distribution, contemporary strain field, and Cenozoic volcanism. *Geosphere* **2009**, *5*, 199–214. [CrossRef]
61. Deng, Q.; Zhang, P.; Ran, Y.; Yang, X.; Min, W.; Chen, L. Active tectonics and earthquake activities in China. *Front. Earth Sci.* **2003**, *10*, 66–73. (In Chinese)
62. Gan, W.; Zhang, P.; Shen, Z.; Niu, Z.; Wang, M.; Wan, Y.; Zhou, D.; Cheng, J. Present-day crustal motion within the Tibetan Plateau inferred from GPS measurements. *J. Geophys. Res. Solid. Earth* **2007**, *112*, B08416. [CrossRef]
63. Zheng, G.; Wang, H.; Wright, T.J.; Lou, Y.; Zhang, R.; Zhang, W.; Shi, C.; Huang, J.; Wei, N. Crustal deformation in the India-Eurasia collision zone from 25 years of GPS measurements. *J. Geophys. Res. Solid. Earth* **2017**, *122*, 9290–9312. [CrossRef]
64. Wessel, P.; Luis, J.F.; Uieda, L.; Scharroo, R.; Wobbe, F.; Smith, W.H.F.; Tian, D. The Generic Mapping Tools version 6. *Geochem. Geophys. Geosyst.* **2019**, *20*, 5556–5564. [CrossRef]
65. Rosen, P.A.; Gurrola, E.; Sacco, G.F.; Zebker, H. The InSAR scientific computing environment. In Proceedings of the 9th European Conference on Synthetic Aperture Radar, Nuremberg, Germany, 23–26 April 2012; pp. 730–733.
66. Fattahi, H.; Agram, P.; Simons, M. A Network-Based Enhanced Spectral Diversity Approach for TOPS Time-Series Analysis. *IEEE Trans. Geosci. Remote Sens.* **2017**, *55*, 777–786. [CrossRef]
67. Chen, C.W.; Zebker, H.A. Two-dimensional phase unwrapping with use of statistical models for cost functions in nonlinear optimization. *J. Opt. Soc. Am. A* **2001**, *18*, 338–351. [CrossRef]
68. Yunjun, Z.; Fattahi, H.; Amelung, F. Small baseline InSAR time series analysis: Unwrapping error correction and noise reduction. *Comput. Geosci.* **2019**, *133*, 104331. [CrossRef]
69. Doin, M.P.; Lodge, F.; Guillaso, S.; Jolivet, R.; Lasserre, C.; Ducret, G.; Grandin, R.; Pathier, E.; Pinel, V. Presentation of the small baseline NSBAS processing chain on a case example: The Etna deformation monitoring from 2003 to 2010 using Envisat data. In Proceedings of the Fringe 2011 Workshop, Frascati, Italy, 19–23 September 2011.
70. Doin, M.P.; Lasserre, C.; Peltzer, G.; Cavalié, O.; Doubre, C. Corrections of stratified tropospheric delays in SAR interferometry: Validation with global atmospheric models. *J. Appl. Geophys.* **2009**, *69*, 35–50. [CrossRef]
71. Jolivet, R.; Grandin, R.; Lasserre, C.; Doin, M.P.; Peltzer, G. Systematic InSAR tropospheric phase delay corrections from global meteorological reanalysis data. *Geophys. Res. Lett.* **2011**, *38*, L17311. [CrossRef]
72. Bagnardi, M.; Hooper, A. Inversion of surface deformation data for rapid estimates of source parameters and uncertainties: A Bayesian approach. *Geochem. Geophys. Geosyst.* **2018**, *19*, 2194–2211. [CrossRef]
73. Watson, A.R.; Elliott, J.R.; Walters, R.J. Interseismic strain accumulation across the Main Recent Fault, SW Iran, from Sentinel-1 InSAR observations. *J. Geophys. Res. Solid Earth* **2022**, *127*, e2021JB022674. [CrossRef]

74. Walters, R.J.; Holley, R.J.; Parsons, B.; Wright, T.J. Interseismic strain accumulation across the North Anatolian fault from envisat InSAR measurements. *Geophys. Res. Lett.* **2011**, *38*, L05303. [CrossRef]
75. Hussain, E.; Hooper, A.; Wright, T.J.; Walters, R.J.; Bekaert, D.P.S. Interseismic strain accumulation across the central North Anatolian fault from iteratively unwrapped InSAR measurements. *J. Geophys. Res. Solid. Earth* **2016**, *121*, 9000–9019. [CrossRef]
76. Hussain, E.; Wright, T.J.; Walters, R.J.; Bekaert, D.P.S.; Lloyd, R.; Hooper, A. Constant strain accumulation rate between major earthquakes on the North Anatolian Fault. *Nat. Commun.* **2018**, *9*, 1392. [CrossRef] [PubMed]
77. Weiss, J.R.; Walters, R.J.; Morishita, Y.; Wright, T.J.; Lazecky, M.; Wang, H.; Hussain, E.; Hooper, A.J.; Elliott, J.R.; Rollins, C.; et al. High-Resolution surface velocities and strain for Anatolia from Sentinel-1 InSAR and GNSS data. *Geophys. Res. Lett.* **2020**, *47*, e2020GL087376. [CrossRef]
78. Aslan, G.; Lasserre, C.; Cakir, Z.; Ergintav, S.; Özarpaci, S.; Dogan, U.; Bilham, R.; Renard, F. Shallow creep along the 1999 Izmit earthquake rupture (Turkey) from GPS and high temporal resolution interferometric synthetic aperture radar data (2011–2017). *J. Geophys. Res. Solid Earth* **2019**, *124*, 2218–2236. [CrossRef]
79. Hao, M.; Wang, Q.; Shen, Z.; Cui, D.; Ji, L.; Li, Y.; Qin, S. Present day crustal vertical movement inferred from precise leveling data in eastern margin of Tibetan Plateau. *Tectonophysics* **2014**, *632*, 281–292. [CrossRef]
80. Wu, Y.; Zheng, Z.; Nie, J.; Chang, L.; Su, G.; Yin, H.; Liang, H.; Pang, Y.; Chen, C.; Jiang, Z.; et al. Highprecision vertical movement and three-dimensional deformation pattern of the Tibetan Plateau. *J. Geophys. Res. Solid Earth* **2022**, *127*, e2021JB023202. [CrossRef]
81. Pan, Y.; Hammond, W.C.; Ding, H.; Mallick, R.; Jiang, W.; Xu, X.; Shum, C.K.; Shen, W. GPS imaging of vertical bedrock displacements: Quantification of two-dimensional vertical crustal deformation in China. *J. Geophys. Res. Solid Earth* **2021**, *126*, e2020JB020951. [CrossRef]
82. Zhao, Q.; Chen, Q.; Dam, T.; She, Y.; Wu, W. The vertical velocity field of the Tibetan Plateau and its surrounding areas derived from GPS and surface mass loading models. *Earth Planet. Sci. Lett.* **2023**, *609*, 118107. [CrossRef]

Disclaimer/Publisher's Note: The statements, opinions and data contained in all publications are solely those of the individual author(s) and contributor(s) and not of MDPI and/or the editor(s). MDPI and/or the editor(s) disclaim responsibility for any injury to people or property resulting from any ideas, methods, instructions or products referred to in the content.